We also note that some (10) fringes are longer and more curved. This is because, in such places, the rod is not precisely perpendicular to the electron beam. The variation of the (10) fringes at various places in one rod means that the rod is not perfectly straight. Figure 5 shows the effect of crystal tilting on the fringes in the TEM image: the image (Fig. 5b) can be closely simulated (Fig. 5c) when the tilting (Fig. 5a) is taken into consideration. It is important to note that all of the (10) fringes are distinctly curved and, furthermore, all the fringes curve in the same direction within one rod. It is confirmed by simulation that rods of right- and left-handedness have oppositely curved (10) fringes when they are tilted to the same direction relative to the electron beam. Therefore, the handedness of the rod may be determined by the direction of curvature of the (10) fringe. The rod observed in the TEM image shown has left-handed chirality.

This type of chiral rod, with mesoporous channels inside, can serve as an interesting container for fabricating chiral metal nanowires. In this work we succeeded in fabricating Co and Pt nanowires within the pores of the chiral mesoporous silica. TEM images (Supplementary Fig. 2) show Co and Pt wires (black contrast) inserted into the chiral channels, although there are also some large metal particles on the outer surface of the rod. Supplementary Fig. 2c shows a schematic drawing of channels with different curvature within which wires were fabricated. The two Co wires indicated by arrows and arrowheads clearly show that the curvatures are different. This is also a clear demonstration that the channels have chirality.

To characterize the enantiomeric purity of the material, CD (circular dichroism) spectra of the synthesis-gel were measured. These spectra showed a CD band around 210–250 nm with positive sign (Supplementary Fig. 3). This CD band is attributed to the chiral micelle, similar to acylglutamate[9], which confirmed the occurrence of ordered, enantiopure self-assembly[10]. No CD band was detected for the synthesis-gel with racemic C_{14}-LD-AlaS (not shown). Handedness of the porous materials was estimated by counting characteristic morphologies from 500 randomly chosen crystals in the SEM images, and left-/right-handed ratios proved to be 6.5/3.5 and 7.5/2.5 for the C_{14}-L-AlaS/TMAPS and C_{14}-L-AlaA/APS synthesis systems, respectively. These findings suggest that competing driving forces for the formation of chiral structure exist, other than the chiral surfactant packing. As a control, a mixture of racemic sodium N-acyl-DL-alanate was also used, resulting in unstable two-dimensional-hexagonal mesoporous silica (the structure was destroyed by calcination) with only a small amount of twisted material formed. The control of enantiopurity and the synthesis mechanism is currently being studied.

To our knowledge, this is the first synthesis of silica crystals with chiral mesopores—which are not soft, but hard materials—by the structure-directing method. Such chiral materials have a clear advantage in their physical strength over chiral liquid-crystal assemblies, yielding a permanent chiral space. Natural chiral imprinting in inorganic structures probably occurs via a similar inorganic/organic chiral interface. □

Methods

Preparation of chiral mesoporous silica

Chiral mesoporous silica was synthesized by using chiral surfactant N-miristoyl-L-alanine sodium salt (C_{14}-L-AlaS) as template, and TMAPS and APS as CSDA. In a typical synthesis, C_{14}-L-AlaS (0.32 g, 1 mmol) was dissolved in deionized water (32 g) with stirring at room temperature. 0.1 M HCl (1.4 g, 0.14 mmol) was added to the surfactant solution under vigorous stirring at room temperature to partially neutralize the salt to produce free amino acid. After the mixture had been stirred for 1 h, a mixture of 1.40 g TEOS and 0.20 g TMAPS (50% in methanol) was added to the mixture with stirring at 22 °C. Then, the mixture was allowed to react at 22 °C under static conditions for 2 h. The chiral mesostructured product thus formed was cured at 80 °C for an additional 15 h. The products were recovered by centrifugal separation and dried at 60 °C. Both the anionic surfactant and the organics of the CSDA used were removed by calcination at 650 °C for 6 h.

Preparation of chiral metal wire

The chiral metal wires were prepared by two-step impregnation, oxidation/reduction procedures, using chiral mesoporous silica as a hard template[11,12]. Typically, 0.15 g chiral mesoporous silica was impregnated with 1.8–2.6 mmol of metal precursors ($Co(NO_3)_2 \cdot 6H_2O$ and $[Pt(NH_3)_4](NO_3)_2$) in total. The Co and Pt precursor was activated while being slowly heated to 350 °C in a stream of O_2, and then reduced with stream of H_2 at 430 °C and 300 °C, respectively.

TEM image simulation

The ideal projected potential of the chiral material, which consists of uniform density walls and empty chiral pores, was constructed. TEM image simulation was performed by using the projected potential (kinematical scattering approximation) and incorporating an absorption effect. The applied objective lens aperture was so small ($\sim 0.5\,nm^{-1}$) that the simulated image should be regarded as a bright-field image.

1. Davis, M. E. New vistas in zeolite and molecular sieve catalysis. *Acc. Chem. Res.* **26**, 111–115 (1993).
2. Gier, T. E., Bu, X., Feng, P. & Stucky, G. D. Synthesis and organization of zeolite-like materials with three-dimensional helical pores. *Nature* **395**, 154–157 (1998).
3. Wang, Y., Yu, J., Guo, M. & Xu, R. [{Zn$_2$(HPO$_4$)$_4$}{Co(dien)$_2$}]·H$_3$O: A zinc phosphate with multidirectional intersecting helical channels. *Angew. Chem. Int. Edn Engl.* **42**, 4089–4092 (2003).
4. Davis, M. E. Ordered porous materials for emerging applications. *Nature* **417**, 813–821 (2002).
5. Baiker, A. Chiral catalysis on solids. *Curr. Opin. Solid State Mater. Sci.* **3**, 86–93 (1998).
6. Che, S. *et al.* A novel anionic surfactant templating route for synthesizing mesoporous silica with unique structure. *Nature Mater.* **2**, 801–805 (2003).
7. Tracey, A. S. & Zhang, X. Investigation into the mechanism for generation of the helical axis in cholesteric lyotropic liquid crystals. *J. Phys. Chem.* **96**, 3889–3894 (1992).
8. Acharya, D. P. *et al.* Phase behavior and effect of enantiomerism on potassium N-dodecanoyl alaninate/water/decanol system. *J. Oleo. Sci.* **52**, 407–420 (2003).
9. Sakamoto, K. & Hatano, M. Formation of chiral aggregation of acylamino acid in solutions. *Bull. Chem. Soc. Jpn* **53**, 339–343 (1980).
10. Iwahashi, M. *et al.* Solvent effect on chiral aggregate formation of acylamino acids. *J. Oleo. Sci.* **51**, 705–713 (2003).
11. Shin, H. J., Ryoo, R., Liu, Z. & Terasaki, O. Template synthesis of asymmetrically mesostructured platinum networks. *J. Am. Chem. Soc.* **123**, 1246–1247 (2001).
12. Tian, B. *et al.* Facile synthesis and characterization of novel mesoporous and mesorelief oxides with gyroidal structures. *J. Am. Chem. Soc.* **126**, 865–875 (2004).

....

Analysing the 1811–1812 New Madrid earthquakes with recent instrumentally recorded aftershocks

Karl Mueller[1], **Susan E. Hough**[2] & **Roger Bilham**[1,3]

[1]*Department of Geological Sciences, University of Colorado, Boulder, Colorado 80309-0399, USA*
[2]*US Geological Survey, 525 South Wilson Ave, Pasadena, California 91030, USA*
[3]*CIRES University of Colorado, Boulder, Colorado 80309-0216, USA*

....

Although dynamic stress changes associated with the passage of seismic waves are thought to trigger earthquakes at great distances, more than 60 per cent of all aftershocks appear to be triggered by static stress changes within two rupture lengths of a mainshock[1–5]. The observed distribution of aftershocks may thus be used to infer details of mainshock rupture geometry[6]. Aftershocks following large mid-continental earthquakes, where background stressing rates are low, are known to persist for centuries[7,8], and models based on rate-and-state friction laws

provide theoretical support for this inference[9]. Most past studies of the New Madrid earthquake sequence have indeed assumed ongoing microseismicity to be a continuing aftershock sequence[10–12]. Here we use instrumentally recorded aftershock locations and models of elastic stress change to develop a kinematically consistent rupture scenario for three of the four largest earthquakes of the 1811–1812 New Madrid sequence. Our results suggest that these three events occurred on two contiguous faults, producing lobes of increased stress near fault intersections and end points, in areas where present-day microearthquakes have been hitherto interpreted as evidence of primary mainshock rupture. We infer that the remaining New Madrid mainshock may have occurred more than 200 km north of this region in the Wabash Valley of southern Indiana and Illinois—an area that contains abundant modern microseismicity, and where substantial liquefaction was documented by historic accounts. Our results suggest that future large midplate earthquake sequences may extend over a much broader region than previously suspected.

Previous studies based on disparate lines of evidence have concluded that the first (NM1, 16 December 1811, magnitude $M = 7.3$) and last (NM3, 7 February 1812, $M = 7.5$) of the four principal New Madrid earthquakes respectively occurred on two well-defined faults, the northeast-striking Cottonwood Grove fault[12,13] and the west-dipping Reelfoot thrust[11,14–17] (Fig. 1). The smaller, second earthquake of the sequence (NM1-A, 16 December 1811, $M = 7.0$) may have occurred on either of these faults, or on a separate fault. The third earthquake (NM2, 23 January 1812, $M = 7.0$) has hitherto been interpreted as a strike–slip rupture on the northern limb of the New Madrid Seismic Zone (NMSZ).

To explore further a rupture scenario for the sequence, we calculated elastic stress changes produced by a sequence of fault ruptures to determine whether they are predicted to inhibit or enhance subsequent rupture of nearby target faults, with appro-

priate sensing of displacement, surface area and orientation. We assumed that the initial shocks triggered subsequent ones and that triggering was caused entirely by static stress changes. In our models we assumed that the end points of the Reelfoot thrust are similar to the extent of fault-related folding of the ground surface in 1812 (ref. 15) that occurs above this fault for ~27 km northeast from its intersection with the Cottonwood Grove fault. Evidence for surface folding above the Reelfoot fault in 1812 includes eyewitness accounts of disruptions to the Mississippi River[16], radiocarbon dating of deformed Holocene sediments[18], and surface geomorphology[17,19]. We assumed that the Cottonwood Grove fault extends southwest of its intersection with the Reelfoot fault[1] (Fig. 1).

Whereas there is little doubt about the locations of NM1 and NM3, the locations of NM1-A and NM2 remain conjectural. We used Coulomb theory[5] to test the plausibility of published rupture scenarios[1] using recent estimates for magnitudes[14] and fault geometry[11]. In our initial model, we assumed 4 m of dextral slip on the Cottonwood Grove fault (NM1, Figs 1, 2a) and 1 m of dextral slip on a 25-km-long northern extension of the same fault (NM1-A). We assign NM2 to a 40-km-long dextral rupture on the northeast-trending arm of microseismicity at the northern end of the NMSZ (Fig. 1), as proposed by previous studies[1]. The final event, NM3, is assumed to release 5 m of slip on the northwest-trending Reelfoot blind thrust fault[18,19] (Fig. 1). We find this sequence scenario problematic because the first two events generate a lobe of reduced Coulomb stress for either dextral or thrust rupture in the region of NM2 (a decrease of 0.2–1.0 bar) that should inhibit faulting here (Fig. 2a).

We next examined alternative fault ruptures that might provide a kinematically consistent scenario for the sequence. Numerous model sequences were examined to test the influence of variations in rupture strike, slip, length, depth and sequence order on the prevailing stress field before each successive large shock (Fig. 2b, c). The results of these calculations suggest that the large thrust rupture on the Reelfoot fault (NM3) was probably triggered by a strike–slip rupture on the Cottonwood Grove fault (NM1), and either a shorter strike–slip rupture at its northern end (Fig. 2b) or a rupture of a short segment of the Reelfoot thrust (Fig. 2c). Our preferred scenario (Fig. 3) includes a 60-km Cottonwood Grove rupture (4 m of dextral slip, NM1), followed by a short rupture on the Reelfoot fault (1 m of reverse slip, NM1-A), and a large rupture on the Reelfoot fault (5 m of reverse slip, NM3).

No models satisfactorily include NM2 as a contiguous rupture, an issue we address in the following section. All consistent models reduce the geometry of the NMSZ to two main faults: the northeast-striking Cottonwood Grove and northwest-striking Reelfoot faults. Coulomb failure models derived from our preferred scenario include lobes of enhanced failure conditions (>1 bar) that correspond to limbs of microseismicity emanating from the three termination points of these two faults (Fig. 3). The lobe of microseismity extending southeast from the intersection of the two faults has puzzled previous investigators because of its lack of surface expression[19], and the requirement that should it represent a contiguous active fault, it must reverse its mechanism during the earthquake cycle[20].

The NM2 mainshock has been the most enigmatic of the four principal events because it was smaller than NM1 and NM3, and documented in fewer eyewitness accounts[15]. Using the method of Bakun and Wentworth[21] we obtained an optimal location at $-88.43°$ W, $36.95°$ N and a magnitude of 6.8 (Fig. 4). The location is not well constrained and can be almost equally well fitted by locations up to 100 km northwest or northeast of the optimal solution. Although the intensity distribution alone cannot rule out a source in the New Madrid region, the strongest shaking during this event was located significantly farther northeast than that from NM1-A, which was almost certainly in the New Madrid
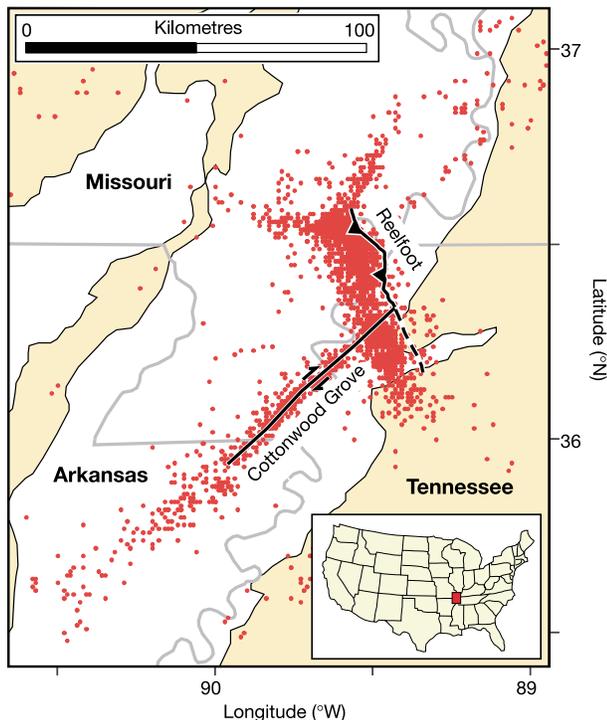
Figure 1 Map of the New Madrid seismic zone as illustrated by microseismicity between 1974 and 1996. The white region is the floodplain of the Mississippi River; grey lines are state boundaries. Locations of the Cottonwood Grove and Reelfoot faults are shown as solid black lines; the southeast extension of the Reelfoot thrust is shown as a dashed line.
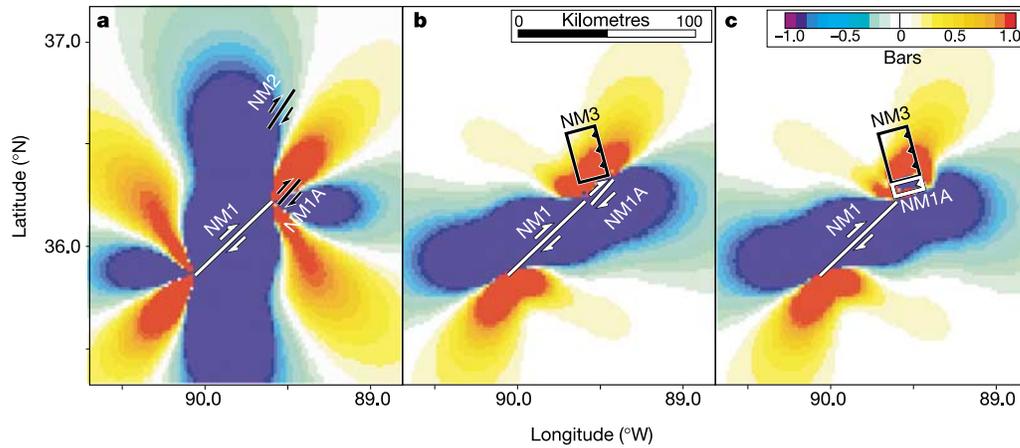
Figure 2 Sequential Coulomb failure stress associated with hypothesized ruptures. All models map stress changes at 12 km, with a coefficient of friction of 0.4 and a maximum principal stress oriented horizontally at N73°E. Earthquakes modelled shown as occurring on source faults (white lines). Black lines denote receiver faults that have not yet slipped during an earthquake. Slip on dextral faults is shown by arrows; barbs denote thrusts. **a**, Coulomb failure enhancement resulting from 4 m of N46°E dextral-shear following rupture during NM1 of the Cottonwood Grove fault for vertical strike–slip faults oriented N34°E. This brings a subsequent event at the northeast end of the Cottonwood Grove fault that might fail during NM1-A closer to failure, but retards failure near the traditional location of NM2. Failure of a dextral fault during NM2 is also inhibited if NM1-A is modelled as a short segment of the Reelfoot thrust. **b**, The Reelfoot thrust (NM3) shown as being brought closer to failure by 4 m of dextral slip during NM1 and 1 m of slip in NM1-A. **c**, The Reelfoot thrust is also brought closer to failure by 4 m of dextral slip during NM1 followed by 1 m of reverse slip on the Reelfoot thrust from NM1-A.

region[1,22]. The intensity distribution suggests that NM2 was a remotely triggered earthquake.

The absence of a high-intensity 'bulls-eye' for NM2 (Fig. 4) is consistent with a location in southeastern Illinois, a region that was very sparsely populated in 1812 (ref. 23). Moreover, had the 1812 event resembled the 1968 $M_b = 5.3$ southern Illinois earthquake, which occurred at 20–25 km depth[24], it would have produced a broad intensity distribution. A location north and east of NM1 and NM3 would explain why remotely triggered earthquakes occurred in northern Kentucky after NM2 (ref. 25), but none were observed following NM1. A southeastern Illinois location could also explain reported liquefaction accounts there[23] (Fig. 4). Our rupture scenario for NM1, NM1-A, and NM3 is also consistent with the observation of three liquefaction events in the New Madrid region in 1811–1812 (ref. 26).

One historic account provides an intriguing suggestion of a possible surface rupture some 220 km from New Madrid. This account, by Yearby Land, described "a big crack [that] was made in the ground" with two feet of vertical displacement to the south[23]. Even in 1858, the feature (38.07° N, 88.11° W) could be traced for a reported distance of two miles. Near this crack Land stated that "piles and piles of pure, snow white sand were heaved up" including some as big as "several wagon loads". Field reconnaissance by the authors verified many of the details in the Land account, and confirmed evidence of sand blows on the surface of the field where they were reported. In addition to providing a clear account of liquefaction, this report appears to describe either surface rupture on an east–west trending fault or substantial ground slumping. None of the earthquakes caused significant damage in the region beyond toppling chimneys, but, in addition to the sparse population, it has been noted that the buildings were all extremely flexible[23]. Land's account does not link the effects to a particular earthquake, and thus has not been used in previous intensity studies. At a minimum, however, it indicates that ground motion severe enough to cause substantial liquefaction occurred during the sequence, in a location centred in the area of highest shaking from NM2. We also note that a linear northwest-trending belt of rapidly occurring microseismicity coincides with this location[27], and that
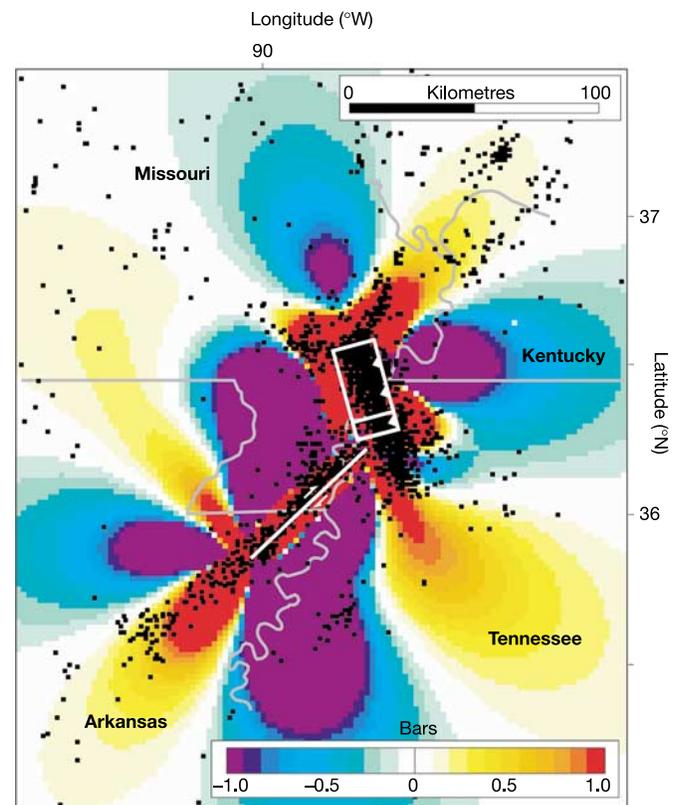
Figure 3 Elastic stress field at 12 km depth produced by NM1, NM1A and NM3 in 1811–1812. Preferred fault ruptures are shown as white lines (NM1, 4 m dextral slip on the 60-km-long Cottonwood Grove fault); a small white rectangle (NM1-A, 1 m reverse slip on Reelfoot thrust); and a large rectangle (NM3, 5 m reverse slip rupture of the Reelfoot thrust). Note the general coincidence of arms of microseismicity with lobes of enhanced stress.
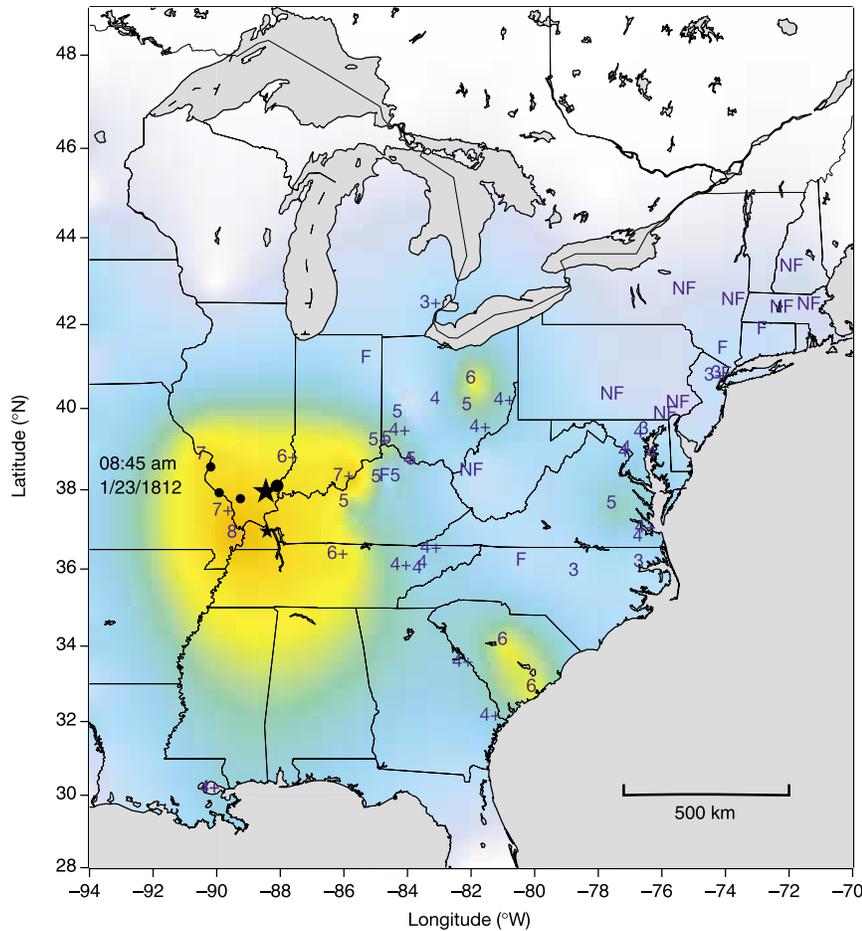
Perceived shaking	Not felt	Weak	Light	Moderate	Strong	Very strong	Severe	Violent	Extreme
Potential damage	None	None	None	Very light	Light	Moderate	Moderate/heavy	Heavy	Very heavy
Peak acceleration (% of g)	<0.17	0.17–1.4	1.4–3.9	3.9–9. 2	9.2–18	18–34	34–65	65–124	>124
Peak velocity (cm s^{-1})	<0. 1	0.1–1. 1	1.1–3. 4	3.4–8. 1	8.1–16	16–31	31–60	60–116	>116
Instrumental intensity	I	II–III	IV	V	VI	VII	VIII	IX	X+

Figure 4 Mercalli intensities inferred for NM2, 23 January 1812, with symbols centred on towns. To map the distribution of shaking we use simple mathematical interpolation[10]. The small star shows the optimal epicentre using quantitative regression[21]; the large star shows the location of the 1968 Southern Illinois earthquake. Black circles correspond to locations where liquefaction was documented during the 1811–1812 sequence. The easternmost and largest circle identifies the location of the White County, Illinois, event, the account of which describes substantial liquefaction as well as surface cracking[23].

the rate of M > 3 earthquakes has previously been quite high in the Wabash Valley.

With the assumption that the principal earthquakes of the 1811–1812 New Madrid sequence constitute a progressively triggered sequence, we conclude that primary faulting in the NMSZ occurred as three ruptures on a linked strike–slip and thrust fault system. The third mainshock, hitherto assigned to a lobe of microseismicity at the north end of the thrust fault, may have been a triggered earthquake more than 200 km northeast of New Madrid in a region of abundant ongoing microseismicity. We interpret diffuse arms of microseismicity now occurring at the end points and intersections of the two main New Madrid faults as aftershocks occurring in regions where stress was increased by the mainshocks. Our interpretation is consistent with established magnitude/fault area results, and do not require exceptionally large fault areas or stress drop values for the New Madrid mainshocks. Ironically, however, the results of this study imply that the hazard associated with mid-continent earthquakes might be more widely distributed than

previously recognized. That is, large dynamically triggered remote earthquakes may follow large mid-plate mainshocks. □

1. Johnston, A. C. & Schweig, E. S. The enigma of the New Madrid earthquakes of 1811–1812. *Annu. Rev. Earth Planet. Sci. Lett.* **24,** 339–384 (1996).
2. Kilb, D., Gomberg, J. & Bodin, P. Triggering of earthquake aftershocks by dynamic stresses. *Nature* **408,** 570–574 (2000).
3. Das, S. & Scholz, C. H. Off-fault aftershock clusters caused by shear-stress increase. *Bull. Seismol. Soc. Am.* **71,** 1669–1675 (1981).
4. Reasenberg, P. A. & Jones, L. M. Earthquake hazard after a mainshock in California. *Science* **243,** 1173–1176 (1989).
5. Toda, S., Stein, R. S., Reasenberg, P. A., Dieterich, J. H. & Yoshida, A. Stress transferred from the 1995 Mw = 6.9 Kobe Japan, shock: Effect on aftershocks and future earthquake probabilities. *J. Geophys. Res.* **103,** 24,543–24,565 (1998).
6. Seeber, L. & Armbruster, J. G. Earthquakes as beacons of stress change. *Nature* **407,** 69–72 (2000).
7. Ebel, J., Bonjer, E. & Oncescu, M. Paleoseismicity: Seismicity evidence for past large earthquakes. *Seismol. Res. Lett.* **71,** 283–294 (2000).
8. Gan, W. & Prescott, W. H. Crustal deformation rates in central and eastern U.S. inferred from GPS. *Geophys. Res. Lett.* **28,** 3733–3736 (2001).
9. Dieterich, J. A constitutive law for rate of earthquake production and its application to earthquake clustering. *J. Geophys. Res.* **99,** 2601–2618 (1994).

287

10. Nuttli, O. W. The Mississippi Valley earthquakes of 1811 and 1812: Intensities, ground motion, and magnitudes. *Bull. Seismol. Soc. Am.* **63**, 227–248 (1973).

11. Mueller, K. & Pujol, J. Three-dimensional geometry of the Reelfoot blind thrust: implications for moment release and earthquake magnitude in the New Madrid seismic zone. *Bull. Seismol. Soc. Am.* **91**, 1563–1573 (2001).

12. Johnston, A. C. Seismic moment assessment of earthquakes in stable continental regions III, New Madrid 1811–1812, Charleston 1886, and Lisbon 1755. *Geophys. J. Int.* **126**, 314–344 (1996).

13. Guccione, M. J., VanArsdale, R. B. & Hehr, L. H. Origin and age of the Manila high and associated Big Lake "sunklands" in the New Madrid seismic zone, northeastern Arkansas. *Geol. Soc. Am. Bull.* **112**, 579–590 (2000).

14. Hough, S. E., Armbruster, J. G., Seeber, L. & Hough, J. F. On the modified Mercalli intensities and magnitudes of the 1811–1812 New Madrid, central United States earthquakes. *J. Geophys. Res.* **105**, 23839–23864 (2000).

15. Baldwin, J. N., Barron, A. D., Kelson, K. I., Harris, J. B. & Cashman, S. Preliminary paleoseismic and geophysical investigation of the north Farrenburg lineament: Primary tectonic deformation associated with the New Madrid North fault? *Seismol. Res. Lett.* **73**, 393–413 (2002).

16. Odum, J. K., Stephenson, W. J., Shedlock, K. M. & Pratt, T. L. Near-surface structural model for deformation associated with the February 7, 1812, New Madrid, Missouri, earthquake. *Geol. Soc. Am. Bull.* **110**, 149–162 (1998).

17. Van Arsdale, R. B., Kelson, K. I. & Lumsden, C. H. Northern extension of the Tennessee Reelfoot scarp into Kentucky and Missouri. *Seismol. Res. Lett* **65**, 57–62 (1995).

18. Kelson, K. I., Simpson, G. D., VanArsdale, R. B., Haraden, C. C. & Lettis, W. R. Multiple late Holocene earthquakes along the Reelfoot fault, central New Madrid seismic zone. *J. Geophys. Res.* **101**, 6151–6170 (1992).

19. Guccione, M. J. *et al.* Stream response to repeated coseismic folding, Tiptonville Dome, western Tennessee. *Geomorph* **43**, 313–349 (2002).

20. Gomberg, J. & Ellis, M. Topography and tectonics of the central New Madrid seismic zone: Results of numerical experiments using a three-dimensional boundary element program. *J. Geophys. Res.* **99**, 20299–20310 (1994).

21. Bakun, W. H. & Wentworth, C. M. Estimating earthquake location and magnitude from seismic intensity data. *Bull. Seismol. Soc. Am.* **87**, 1502–1521 (1997).

22. Hough, S. E. & Martin, S. Magnitude estimates of two large aftershocks of the 16 December 1811 New Madrid earthquake. *Bull. Seismol. Soc. Am.* **92**, 3259–3268 (2002).

23. Berry, D. L. The Illinois earthquake of 1811 and 1812. *Illinois State Hist. Soc. Trans.* **12**, 74–78 (1908).

24. Stauder, W. & Nuttli, O. W. Seismic studies—south-central Illinois earthquake of November 9, 1968. *Bull. Seismol. Soc. Am.* **60**, 973–981 (1970).

25. Hough, S. E. Triggered earthquakes and the 1811–1812 New Madrid, central U.S. earthquake sequence. *Bull. Seismol. Soc. Am.* **91**, 1574–1581 (2001).

26. Tuttle, M. P. The use of liquefaction features in paleoseismology: Lessons learned in the New Madrid seismic zone, central United States. *J. Seismol.* **5**, 361–380 (2001).

27. Pavlis, G. L., Rudman, A. J., Pope, B. P., Hamburger, M. W. & Bear, G. W. Seismicity of the Wabash Valley seismic zone based on a temporary seismic array experiment. *Seismol. Res. Lett.* **73**, 751–761 (2002).

··

Articulated Palaeozoic fossil with 17 plates greatly expands disparity of early chitons

Michael J. Vendrasco[1], Troy E. Wood[3] & Bruce N. Runnegar[1,2]*

[1]*Department of Earth and Space Sciences,* [2]*Institute of Geophysics and Planetary Physics and Molecular Biology Institute, University of California, Los Angeles, California 90095, USA*
[3]*Department of Biology, JH 142, 1001 E. Third Street, Indiana University, Bloomington, Indiana 47405, USA*

* *Present address: NASA Astrobiology Institute, MS 240-1, Ames Research Center, Moffett Field, California 94035, USA*

···

Modern chitons (Mollusca: Polyplacophora) possess a highly conserved skeleton of eight shell plates (valves) surrounded by spicules or scales, and fossil evidence suggests that the chiton skeleton has changed little since the first appearance of the class in the Late Cambrian period (about 500 million years before present, Myr BP). However, the Palaeozoic problematic taxon Multiplacophora[1–5], in spite of having a more complex skeleton, shares several derived characters with chitons. The enigmatic status of the Multiplacophora is due in part to the fact that its members had an exoskeleton of numerous calcium carbonate valves that usually separated after death. A new articulated specimen from the Carboniferous period (about 335 Myr BP) of Indiana reveals that multiplacophorans had a dorsal protective surface composed of head and tail valves, left and right columns of overlapping valves (five on each side), and a central zone of five smaller valves, all surrounded by an annulus of large spines. Here we describe and name the articulated specimen and present evidence that multiplacophorans were chitons. Thus the highly conserved body plan of living chitons belies the broad disparity of this clade during the Palaeozoic era.

The modern chiton skeleton consists of one column of eight calcareous shell plates (valves) surrounded by a ring of scales or spicules. Articulated fossil chitons share this skeletal body plan. Moreover, isolated fossil valves assigned to the Polyplacophora show bilateral symmetry, consistent with a single column of valves. Consequently, the skeletal morphology of this clade has been interpreted as evolutionarily static, with little change since its origin in the Cambrian[6].

A new, exceptionally preserved multiplacophoran (Fig. 1a) from the Carboniferous of Indiana allows us to link this group with the chitons, and reveals that this clade exhibited far greater skeletal variation during the Palaeozoic than is generally believed. Multiplacophorans (Devonian to Permian, ~380–265 Myr BP, fossils from North America) have been considered problematic in part because the detailed nature of their skeleton was unknown. The new fossil reveals that the multiplacophoran skeleton consists of three longitudinal columns of shell plates plus a head and tail plate, surrounded by elongate, hollow spines (Fig. 1c), an arrangement similar to that of a recently described Ordovician chiton *Echinochiton dufoei*[7]. The *Echinochiton* skeleton consists of a central column of eight valves, two flanking columns of small, dorsally projecting 'scutes', and a girdle harbouring eight pairs of elongate, hollow spines that grew by marginal accretion. Thus, the skeleton of *Echinochiton* is intermediate in form between those of multiplacophorans and typical chitons.

Multiplacophorans share with other chitons an iterated sequence of overlapping, calcareous, marginally accreted valves, surrounded by an armoured girdle. In both groups the anterior and posterior valves are morphologically distinct from the intervening valves; the valve surfaces are porous, and an inner shell layer (articulamentum) projects from the growing margins of valves (Fig. 2a, c). In addition, microscopic canal systems occur within the valves of both taxa (Fig. 2b, d). These tubular canals exist at the interface of two shell layers; numerous, equally spaced canals branch off obliquely towards the surface, and, in certain areas, vertical canals pass through all shell layers[5,8]. In chitons, these canals house tissues that connect sensory structures, known as aesthetes, at the valve surface to the body below[8]. We envisage a similar function for the canals in multiplacophoran valves.

Despite these similarities, multiplacophorans are distinct from typical chitons. Multiplacophorans have three anterior–posterior columns of valves and a sevenfold rather than eightfold iteration of major skeletal elements. In addition, the large, hollow, lateral spines of multiplacophorans are probably not homologous with the small, solid, girdle spicules of chitons, and, conversely, they share many similarities with chiton valves[5,9]. These similarities, which include a porous surface, internal canals, projections of the articulamentum and growth by marginal accretion, suggest that the spines may instead be homologous with chiton valves.

An elementary cladistic analysis strongly supports the placement of multiplacophorans within the total group Polyplacophora (Fig. 3). All modern chiton valves possess projections of the articulamentum (articulaments) that serve to anchor the valves in